bioRxiv preprint doi: https://doi.org/10.1101/2021.05.16.444253; this version posted May 17, 2021. The copyright holder for this preprint (which was not certified by peer review) is the author/funder, who has granted bioRxiv a license to display the preprint in perpetuity. It is made available under aCC-BY-NC-ND 4.0 International license.

Beyond BOLD: in search of genuine diffusion fMRI contrast in human brain

Wiktor Olszowy[1,2,*], Yujian Diao[1,2,3] and Ileana O. Jelescu[1,2,*]

[1] Animal Imaging and Technology, EPFL, Lausanne, Switzerland
[2] CIBM Center for Biomedical Imaging, Switzerland
[3] Laboratoire d'Imagerie Fonctionnelle et Métabolique, EPFL, Lausanne, Switzerland
* corresponding authors

Correspondence and requests for materials should be addressed to W.O. (olszowyw@gmail.com) and I.O.J. (ileana.jelescu@epfl.ch)

Abstract

Functional Magnetic Resonance Imaging (fMRI) is an essential method to measure brain activity non-invasively. While fMRI almost systematically relies on the blood oxygenation level-dependent (BOLD) contrast, there is an increasing interest in alternative methods that would not rely on neurovascular coupling. A promising but controversial such alternative is diffusion fMRI (dfMRI), which relies instead on dynamic fluctuations in apparent diffusion coefficient (ADC) due to microstructural changes underlying neuronal activity. However, it is unclear whether genuine dfMRI contrast, distinct from BOLD contamination, can be detected in the human brain in physiological conditions. Here, we present the first dfMRI study in humans attempting to minimize all BOLD contamination sources and comparing functional responses at two field strengths (3T and 7T), both for task and resting-state (RS) fMRI. Our study benefits from unprecedented high spatiotemporal resolution and harnesses novel denoising strategies. We report task-induced decrease in ADC with temporal and spatial features distinct from the BOLD response and yielding more specific activation maps. Furthermore, we report dfMRI RS connectivity which, compared to its BOLD counterpart, is essentially free from physiological artifacts and preserves positive correlations but preferentially suppresses anti-correlations, which are likely of vascular origin. A careful acquisition and processing design thus enable the detection of genuine dfMRI contrast on clinical MRI systems. As opposed to BOLD, diffusion functional contrast could be particularly well suited for low-field MRI.

bioRxiv preprint doi: https://doi.org/10.1101/2021.05.16.444253; this version posted May 17, 2021. The copyright holder for this preprint (which was not certified by peer review) is the author/funder, who has granted bioRxiv a license to display the preprint in perpetuity. It is made available under aCC-BY-NC-ND 4.0 International license.

Introduction

Functional MRI (fMRI) has become an invaluable tool for neuroscience and is nearly omnipresent in studies of healthy and diseased brain. The most widely used fMRI contrast originates from changes in venous blood oxygenation underlying neuronal activity, also known as BOLD (blood oxygenation level-dependent) signal (Ogawa et al., 1992), to the extent that *"fMRI"* and *"BOLD fMRI"* have become near-synonyms. However, within the BOLD mechanism also lies the major drawback of this contrast: it relies on neurovascular coupling instead of direct neuronal activity. This additional convolution layer has several dramatic implications (Turner, 2016): loss in spatial and temporal specificity, since neuronal activity is convolved with a slow hemodynamic response function, and strong BOLD signal stems not from the locus of neuronal firing, but from nearby venules and veins (Shmuel et al., 2007), a challenging distinction between neuronal and vascular alterations, of relevance to healthy aging or pathology such as tumors and multiple sclerosis (West et al., 2019; Pak et al., 2017; Caprio et al., 2016) and low sensitivity in white matter (Gore et al., 2019; Grajauskas et al., 2019), where vasculature and metabolism are reduced. In addition, BOLD is by design sensitive to fluctuations in local magnetic field homogeneity, which can have numerous sources other than blood oxygenation changes. In other words, BOLD fMRI is also notoriously corrupted by physiological noise. Although a battery of processing tools has been developed to correct for these effects, BOLD functional connectivity studies are still mainly used to inform about population differences and exhibit very limited diagnostic performance at the single-subject level (Dubois and Adolphs, 2016).

Diffusion functional MRI (dfMRI) was proposed as a functional contrast which does not rely on neurovascular coupling (Le Bihan et al., 2006) but instead on the sensitivity of the apparent diffusion coefficient (ADC) of water to dynamic microstructure fluctuations that typically occur in neurons and astrocytes (including their processes) as a result of neuronal activity (Andrew and Macvicar, 1994; Lang et al., 1998; Sherpa et al., 2016). Indeed, diffusion MRI (dMRI) encodes the mean displacement of water molecules, which is on the order of a few microns and is largely governed by the layout of cellular membranes, compartment sizes and other features of tissue microarchitecture. Since the initial work by Le Bihan *et al*., a body of conflicting evidence has been published. Several studies have reported improved temporal and spatial specificity of the dfMRI signal compared to BOLD (Darquie et al., 2001; Tsurugizawa et al., 2013; Nunes et al., 2019) and specificity to neuronal activity rather than vascular response (Flint et al., 2009; Tirosh and Nevo, 2013; Abe et al., 2017). Other works have argued on the contrary that the so-called dfMRI signal is based on residual vascular rather than neuronal contrast and that the method is otherwise not sensitive enough to detect physiological levels of brain activity on an individual basis (Miller et al., 2007; Jin and Kim, 2008; Autio et al., 2011; Bai et al., 2016). The conflicting literature suggests that achieving genuine dfMRI contrast constitutes a true methodological challenge (**Figure 1**).

Briefly, there are three main mechanisms by which the hemodynamic response to neuronal activity can interfere with the dfMRI contrast, with careful solutions to mitigate them (**Figure 1**, **Table 1**). First, the diffusion-weighted MRI signal is, by design of the spin-echo sequence, also T_2-weighted (or T_2*-weighted, for gradient-echo sequences). Changes in tissue T_2* due to blood oxygenation differences between rest and active states are the very mechanism behind the BOLD contrast. Thus, a plain diffusion-weighted signal is also heavily affected by the same mechanism. This confound was present, among others, in Le Bihan et al., 2006; Miller et al., 2007; Autio et al., 2011; Tsurugizawa et al., 2013. Therefore, the ADC time-course should be considered instead – estimated, for instance, from consecutive measurements with two different *b*-values, assuming T_2 to be constant during these two measurements. Second, blood oxygenation dependent field homogeneity implies background field

bioRxiv preprint doi: https://doi.org/10.1101/2021.05.16.444253; this version posted May 17, 2021. The copyright holder for this preprint (which was not certified by peer review) is the author/funder, who has granted bioRxiv a license to display the preprint in perpetuity. It is made available under aCC-BY-NC-ND 4.0 International license.

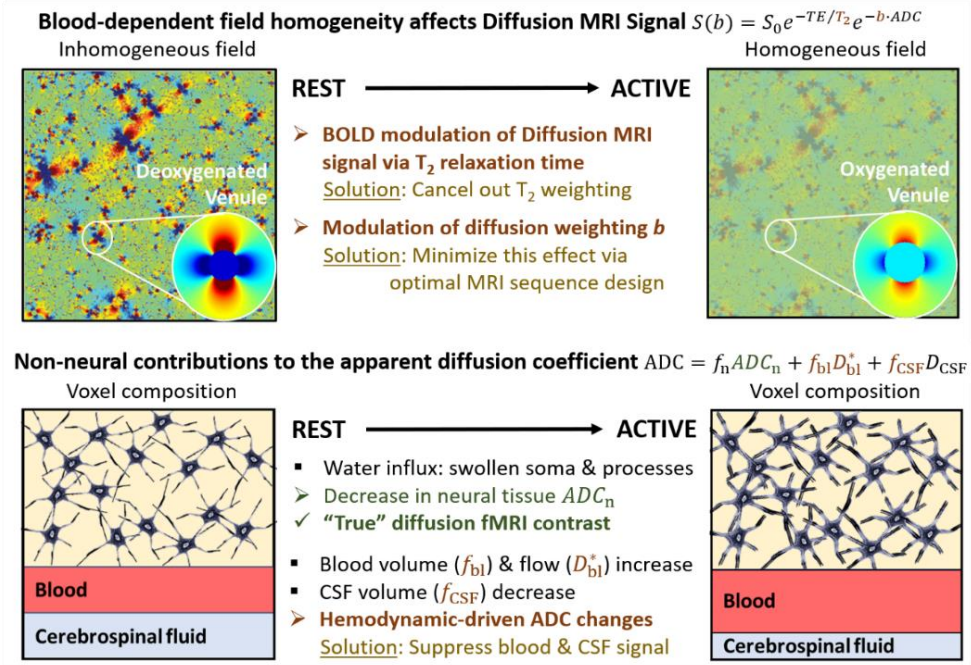

Figure 1. Vascular confounds in dfMRI. Pathways for wanted dfMRI contrast (green font) and for unwanted *"contamination"* of dfMRI neuronal contrast by the same changes in blood oxygenation underlying the BOLD contrast (red font) and solutions to minimize them. Top panels adjusted from Miller and Jezzard, 2008 (Copyright © 2008 Wiley-Liss, Inc.).

gradients $\mathbf{G}_s$ vary with the hemodynamic response. These gradients can contribute to the effective diffusion-weighting imparted in the sequence, most notably via cross-terms with the diffusion gradients $\mathbf{G}_d$. Contributions from background gradients may have challenged the interpretation in Darquie et al., 2001; Autio et al., 2011; Luca et al., 2019. A sequence design that minimizes cross-terms should be preferred, e.g. a twice-refocused spin-echo. Third, the ADC at the voxel level is a combination of diffusivities from all voxel constituents: compartments of interest (intra- and extra-neuronal space), but also blood. The hemodynamic response translates into an increase in blood volume and flow (pseudo-diffusion coefficient D_{bl}*). Blood water contributions to the MRI signal should therefore be eliminated to access changes in tissue ADC only. The inclusion of b=0 in the ADC estimation may result in BOLD-like response functions as, for instance, reported in Luca et al., 2019 and Nunes et al., 2019. It is noteworthy that techniques to suppress the blood signal by injection of magnetic particles (Jin and Kim, 2008) may also introduce an indirect vascular contribution, as they generate susceptibility gradients around vessels that fluctuate with changes in vessel size.

Encouragingly, studies of perfused tissues without vasculature have clearly demonstrated that neuronal activity decreases the overall diffusion coefficient (Flint et al., 2009; Tirosh and Nevo, 2013; Spees et al., 2018), although the sensitivity to physiological levels of activity has been questioned (Bai et al., 2016). New approaches of ultra-high temporal resolution to separate early dfMRI from later BOLD effects have nonetheless singled out genuine dfMRI contrast in the rodent (Nunes et al., 2021, 2019).

We adopt a dfMRI study design that minimizes the aforementioned sources of vascular contamination to determine whether genuine diffusion fMRI contrast is detectable in the human brain at the individual level. A bipolar gradient diffusion sequence was used to mitigate cross-terms between diffusion and susceptibility gradients, and apparent diffusion coefficient (ADC) time-courses were computed using *b*-

bioRxiv preprint doi: https://doi.org/10.1101/2021.05.16.444253; this version posted May 17, 2021. The copyright holder for this preprint (which was not certified by peer review) is the author/funder, who has granted bioRxiv a license to display the preprint in perpetuity. It is made available under aCC-BY-NC-ND 4.0 International license.

Table 1. Explicit mechanisms for vascular contamination of dfMRI contrast, either via the diffusion-weighted signal (Items 1 – 2) or the compartment contributions to the voxel ADC (Items 3 – 4) and technical solutions to address them.

	Sources of vascular contamination	Solution
1	Intrinsic T_2-weighting in diffusion-weighted signal: $S = M_0 e^{-TE/T_2} e^{-b \cdot ADC}$	Calculate ADC time-courses from interleaved acquisition of two *b*-values to cancel out T_2 weighting: $ADC(t) = ln\left(\frac{S_2(t+\delta t)}{S_1(t)}\right)\frac{1}{b_1 - b_2}$
2	Modulation of effective *b*-value by cross-terms between venous background field gradients $G_s(t)$ and diffusion gradients G_D: $b = xG_D^2 + yG_D \cdot G_s(t) + zG_s^2(t)$ Coefficients x, y, z are sequence-dependent. Typically $G_D \gg G_s$.	Diffusion gradient waveform design that minimizes cross-terms e.g. twice-refocused spin-echo
3	Contribution of blood water pool	Operate at *b*-values ≥ 0.2 ms/μm^2 to suppress fast moving spins (blood signal)
4	CSF volume shrinkage to compensate for blood volume increase	Selectively null CSF signal using inversion module

values ≥ 0.2 ms/μm^2 to suppress T_2-weighting and blood pool contributions. We explore different approaches to assessing residual vascular contributions by comparing the dfMRI signal properties at two field strengths, 3T and 7T. From a biophysical standpoint, the dfMRI response should be field-independent while the BOLD magnitude increases with field strength. Finally, we evaluate dfMRI properties not only in response to a task but also, for the first time, in terms of resting-state functional connectivity (RS-FC) compared to T_2-BOLD. The notoriously low sensitivity of dfMRI is balanced by recent improvements in spatio-temporal resolution of the acquisition (e.g. stronger gradients on clinical systems and multi-slice acceleration) and in image pre-processing, in particular Marchenko-Pastur PCA (MP-PCA) denoising (Veraart et al., 2016; Ades-Aron et al., 2021; Diao et al., 2021) to boost the temporal signal-to-noise ratio (tSNR).

Methods

Experimental

The study was examined and approved by the ethics committee of the canton of Vaud (CER-Vaud). Data were acquired on Siemens Magnetom 7T and Prisma 3T scanners, on 22 subjects (7 males, age 25 ± 5). All subjects gave informed written consent after the experimental procedures were explained and prior to enrollment. Four scanning protocols were used: (1) SE-EPI yielding T_2-BOLD contrast, (2) DW-TRSE-EPI with pairs of *b*-values 0.2 and 1 ms/μm^2, (3) DW-TRSE-EPI but with *b*-values 0 and 1, and (4) DW-SE-EPI (monopolar gradient pulses) with *b*-values 0.2 and 1. Sequences were obtained from the Center for Magnetic Resonance Research of the University of Minnesota (https://www.cmrr.umn.edu/multiband/, Uğurbil et al., 2013). All scanning was performed with GRAPPA=2 and Multiband=2 acceleration. Sequence parameters and the numbers of datasets are collected in **Table 2** for each protocol, field strength and scan type (task or resting-state). Due to specific absorption rate limits at 7T, images for some volunteers were acquired with fewer slices than the default of 16. While most of the task datasets were acquired at an isotropic resolution of 2.5 mm, the first datasets had an isotropic resolution of 2 mm. The voxel size was increased in order to improve the SNR.

bioRxiv preprint doi: https://doi.org/10.1101/2021.05.16.444253; this version posted May 17, 2021. The copyright holder for this preprint (which was not certified by peer review) is the author/funder, who has granted bioRxiv a license to display the preprint in perpetuity. It is made available under aCC-BY-NC-ND 4.0 International license.

Table 2. Acquisition parameters for the four protocols.

		(1) SE BOLD		(2) ADC from *b*=0.2/1, bipolar		(3) ADC from *b*=0/1, bipolar		(4) ADC from *b*=0.2/1, monopolar	
		3T	7T	3T	7T	3T	7T	3T	7T
Task	# Datasets	5	8	19	13	1	2	8	8
	TE (ms)	73	65	72	62	72	65	72	62
	TR (s)	1							
	Matrix	94x94					116x116	94x94	
	Resolution (mm^2)	2.5x2.5					2x2	2.5x2.5	
	Slices	16							
	Thickness (mm)	2.5					2	2.5	
	Total volumes	600							
Resting-state	# Datasets	10	10	12	11	0	2	5	5
	TE (ms)	73	65	73	65		65	73	65
	TR (s)	1							
	Matrix	116x116							
	Resolution (mm^2)	2x2							
	Slices	16							
	Thickness (mm)	2							
	Total volumes	600							

All resting-state datasets were acquired at an isotropic resolution of 2 mm. A few dfMRI task datasets were acquired with separate runs to increase the temporal resolution, so that each *b*-value was employed in a separate run. ADC was then calculated from the two separate acquisition runs. Such acquisition enables the temporal resolution of the ADC map to be the same as in the original DW-SE-EPI map. However, this design was found to be rather detrimental in terms of large-scale fluctuations that did not enable the time-courses to be used for an ADC computation, with little benefit/insight brought by higher temporal resolution. For most of the dfMRI acquisitions (13 out of 22 subjects), the *b*-values were alternating within one acquisition run. This way, the temporal resolution of the ADC map was half the temporal resolution of the original DW-SE-EPI map – the repetition time (TR) in the ADC map was twice the TR in the original map. The scanning time for each protocol was approximately 10 minutes. For task datasets, the imaging slab was chosen such that both the visual and motor cortices would be covered. For resting-state datasets, the imaging slab covered the prefrontal cortex and the posterior cingulate cortex, which are crucial elements of the default mode network (Raichle et al., 2001). To be able to later correct the susceptibility distortions using *topup* (Andersson et al., 2003), EPI images with opposite phase encoding directions were acquired. Besides the functional scans, for each subject and at each scanner, an anatomical 1 mm isotropic T_1-weighted image was acquired using an MPRAGE sequence.

For the task runs, subjects were viewing a flashing checkerboard (8 Hz) and concurrently finger-tapping with both hands for 12s following 18s of rest. This boxcar paradigm was implemented using PsychoPy (Peirce et al., 2019). For the resting-state runs, subjects were told to fixate on the cross in the middle of the screen and to relax.

Processing

The processing pipeline is sketched in **Figure 2**.

Outlier detection and removal: Signal drop-outs were observed for some volumes along the time-course, either due to scanner instabilities or motion. To minimize their effect, we implemented a method to automatically detect volume outliers and to replace the signal in such volume outliers with a linearly

bioRxiv preprint doi: https://doi.org/10.1101/2021.05.16.444253; this version posted May 17, 2021. The copyright holder for this preprint (which was not certified by peer review) is the author/funder, who has granted bioRxiv a license to display the preprint in perpetuity. It is made available under aCC-BY-NC-ND 4.0 International license.

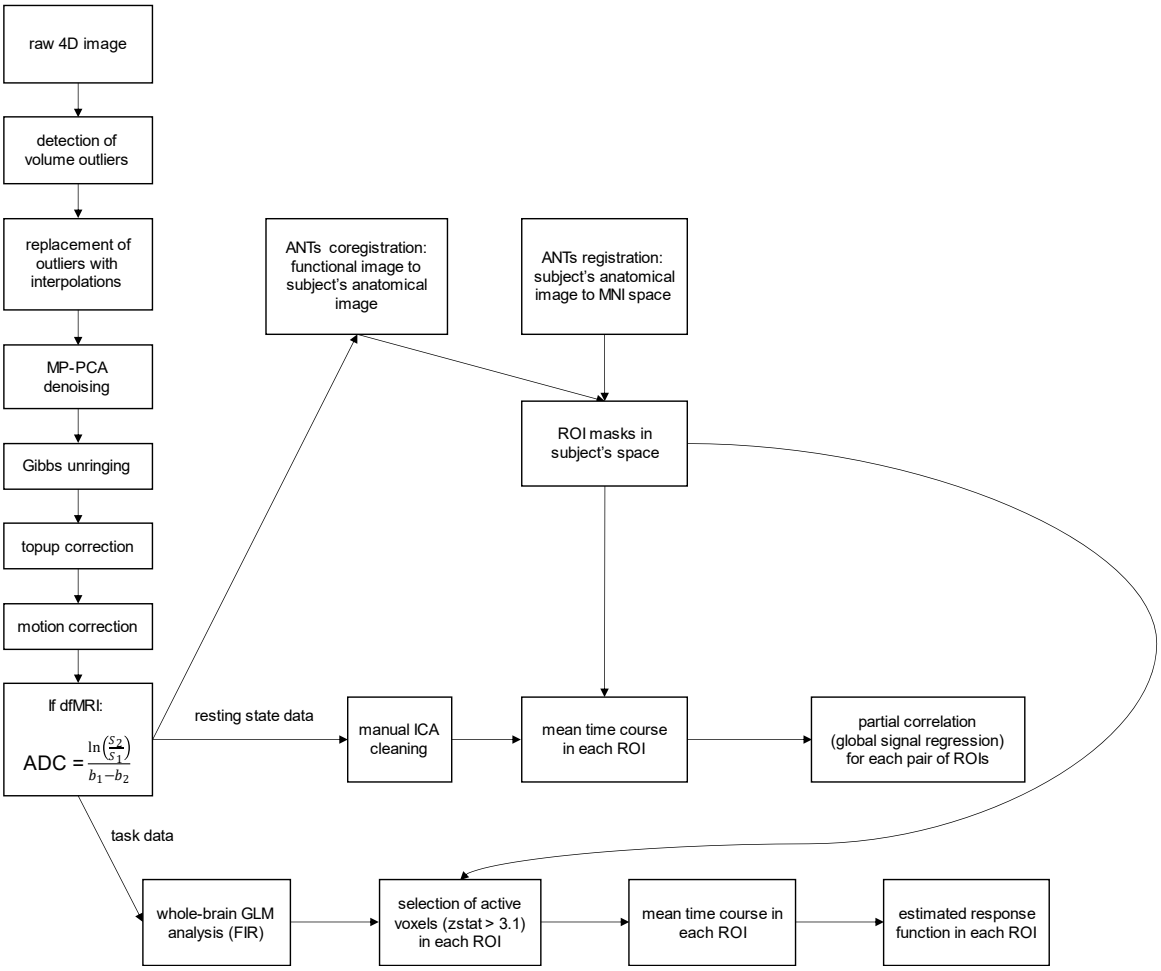

Figure 2. The employed processing pipeline. Data pre-processing included denoising (Veraart et al., 2016; Ades-Aron et al., 2021), Gibbs unringing (Kellner et al., 2016) and corrections for susceptibility distortion (Andersson et al., 2003) and motion. For the apparent diffusion coefficient (ADC) calculation, S_i is the signal level measured with diffusion-weighting b_i.

interpolated signal. A volume was considered an outlier if its detrended average signal over the entire brain was away from the median across all the volumes by more than a pre-specified fraction of this median. This threshold fraction was set at 1% and 3% for 3T and 7T, respectively. It should be noted that after whole-brain averaging, 1 – 3% deviations are much larger than any BOLD fluctuations within this range at the individual voxel level. As low-frequency drifts could affect the detection of volume outliers, the signal was first linearly detrended to identify outliers. For further pre-processing, however, the non-detrended data with outlier exclusion were used. In most cases, the fraction of outliers did not exceed 5%. If this fraction was above 20%, the entire dataset was excluded from further analyses. For the diffusion datasets, the above procedure was employed on volume series corresponding to the two *b*-values separately. **Supplementary Figure 1** presents the above procedure for an exemplary dataset.

Denoising: Data were then denoised using the MP-PCA method (Veraart et al., 2016; Ades-Aron et al., 2021) with a sliding window kernel of 5x5x5 voxels. For the diffusion datasets, the denoising procedure was performed on volume series corresponding to the two *b*-values separately. The residuals were inspected for Gaussianity to verify that the denoising procedure did not alter data distribution properties.

Artifact corrections: Corrections were applied for the Gibbs ringing artifact (Kellner et al., 2016) and the susceptibility distortions (Andersson et al., 2003). For the latter, FSL's tool *topup* was run with settings taken from the UK BioBank study (Alfaro-Almagro et al., 2018). Motion correction was performed with SPM (Friston et al., 1995; Friston, 2007). For the diffusion datasets, motion correction

bioRxiv preprint doi: https://doi.org/10.1101/2021.05.16.444253; this version posted May 17, 2021. The copyright holder for this preprint (which was not certified by peer review) is the author/funder, who has granted bioRxiv a license to display the preprint in perpetuity. It is made available under aCC-BY-NC-ND 4.0 International license.

was performed on volume series corresponding to the two *b*-values separately. Afterwards, the two series were aligned with each other using ANTs rigid transformation (Avants et al., 2011, 2010).

As the last stage of the pre-processing of the diffusion data, ADC maps were calculated as:

$$\mathrm{ADC} = \frac{\ln\left(\frac{S_2}{S_1}\right)}{b_1 - b_2}$$

where S_i is the signal level measured with diffusion-weighting b_i. The later dfMRI task and resting-state analyses employed the quantitative ADC maps. However, the dfMRI volumes acquired at the lower *b*-value (0.2 ms/μm^2) were also used independently as an approximation for SE BOLD – in the following, these datasets are called *"pseudo SE BOLD"*. These pseudo SE BOLD time-courses had the advantage of being directly comparable to the matching ADC time-courses due to their concomitance in time, with identical physiological conditions and brain activity in the volunteer.

For task datasets, our main goal was to compare response functions across the modalities and field strengths. For resting-state datasets, our main goal was to compare functional connectivity matrices, also both across the modalities and field strengths.

Both task and resting-state analyses were performed in subject's spaces to minimize the effect of interpolations on the results. All the associated registration was done with ANTs (Avants et al., 2011, 2010). Following brain extraction, the subject's anatomical image was registered to the Montreal Neurological Institute (MNI) template at 1 mm isotropic resolution using symmetric normalization (SyN). The mean functional image was registered to the subject's anatomical image using rigid transformation. For diffusion data, the mean functional image was calculated for the lower *b*-value volumes only, as these correspond to higher SNR. No spatial smoothing was applied to the maps to enable the investigation of fine spatial differences (Polimeni et al., 2018).

The visual and motor cortices in MNI space were defined using the 1.5 mm isotropic Neuromorphometrics atlas (*Neuromorphometrics, Inc.*). The visual cortex was the sum of the calcarine cortex, occipital pole, superior occipital gyrus, inferior occipital gyrus, cuneus, lingual gyrus, middle occipital gyrus and occipital fusiform gyrus. The motor cortex was the sum of the precentral gyrus medial segment, precentral gyrus and supplementary motor cortex. All the regions were considered bilaterally. Using the above-obtained transformations, the two MNI-defined regions of interest (ROIs) were brought to subject's functional spaces.

For task images, whole-brain general linear model (GLM) analyses were performed in FSL (Jenkinson et al., 2012), using the Finite Impulse Response (FIR) method (Henson et al., 2001) to find activations without making assumptions about the shape of the responses. Both for the SE BOLD and dfMRI analyses, FIR was used with seven basis functions covering 30s of the post-stimulus-onset time. To account for possible low-frequency drifts in the data, a high-pass filter with a cutoff of 1/100 Hz was applied, both on the data and the model. *F*-tests were run on the FIR basis functions and *F*-statistics were transformed into *z*-statistics. For each fMRI dataset and each of the two ROIs, the response function was estimated as the average signal across the trials and the voxels with *z*-statistic > 3.1. If at least 20 voxels in the ROI had a *z*-statistic > 3.1, the estimated response function was taken to the group analysis. For the calculation of group averages, subject-level estimates were normalized to their baseline levels.

For each resting-state dataset, the available ROIs from the Neuromorphometrics atlas were considered. As the acquisitions covered only part of the brain, only some ROIs from the atlas were covered. ROIs for which a coverage of ten or fewer voxels was available were omitted. Pair-wise Pearson correlation coefficients were calculated between the mean time-courses across each ROI. The correlation

bioRxiv preprint doi: https://doi.org/10.1101/2021.05.16.444253; this version posted May 17, 2021. The copyright holder for this preprint (which was not certified by peer review) is the author/funder, who has granted bioRxiv a license to display the preprint in perpetuity. It is made available under aCC-BY-NC-ND 4.0 International license.

coefficients were calculated following global signal regression (GSR), manual independent component analysis (ICA) cleaning (Beckmann and Smith, 2004; Griffanti et al., 2017; Diao et al., 2021) or both. Group analyses were done averaging the resting-state functional connectivity matrices across the subjects. Only ROIs covered by all subjects were considered at the group level.

Results

The outlier ratio was exceeded for six datasets, which were excluded from the analyses. Two resting-state datasets were excluded due to inconsistent positioning of the imaging slab. Data from one subject was excluded entirely because of poor task compliance. Finally, five datasets were excluded because of image artifacts. **Table 2** specifies the numbers of datasets retained for the analyses (N=64 total for task, and N=55 total for resting-state, all protocols combined).

The relatively short TR of 1 second, chosen in the interest of high temporal resolution, yielded limited steady-state signal and SNR. However, the MP-PCA denoising procedure nearly doubled the tSNR (**Supplementary Figure 2**).

Task fMRI

Figure 3 shows group-level activation maps resulting from Protocols (1) and (2) at each field strength. Activation in the visual and motor cortices was observed, both with SE BOLD and with dfMRI, at 3T

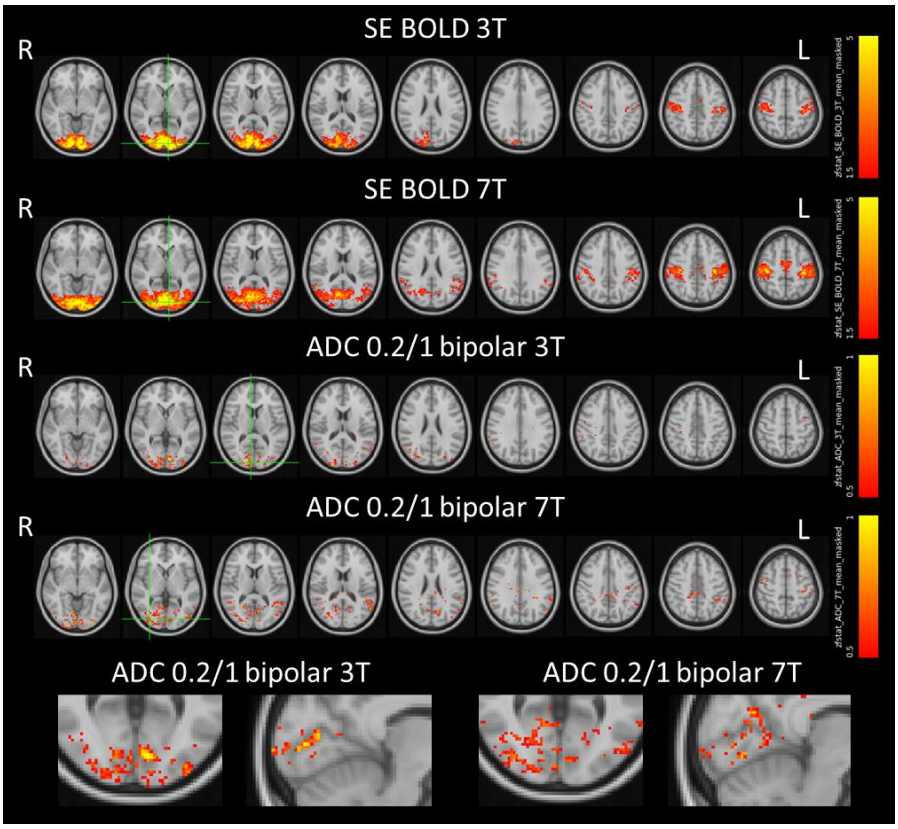

Figure 3. Whole-brain group-averaged *z*-statistic maps for SE BOLD and dfMRI, at 3T and 7T. To find task-induced activation without making assumptions about the shape of the response functions, a Finite Impulse Response (FIR) set was used. Significance was assessed with *F*-tests. The *F*-statistics were converted to *z*-statistics, which these group average maps refer to. Activation both in the visual and motor cortices was observed, both with SE BOLD and with dfMRI, at both fields.

bioRxiv preprint doi: https://doi.org/10.1101/2021.05.16.444253; this version posted May 17, 2021. The copyright holder for this preprint (which was not certified by peer review) is the author/funder, who has granted bioRxiv a license to display the preprint in perpetuity. It is made available under aCC-BY-NC-ND 4.0 International license.

and 7T. While the sensitivity of dfMRI is expectedly lower, its activation patterns point towards improved specificity: the voxels consistently active at the group-level delineate cortical ribbons in the visual area, interhemispheric supplementary motor area and bilateral motor/somatosensory cortices.

Analysis of the group-averaged response functions **(Figure 4**) revealed, as expected, a positive SE BOLD response with an amplitude larger at 7T than at 3T (2% vs. 1% in the visual cortex), as well as a delayed BOLD onset with respect to stimulus and even more delayed return to baseline after stimulus end. It should be noted that these BOLD amplitudes are expectedly lower for T_2-BOLD than for the more familiar T_2*-BOLD. Our optimized dfMRI protocol revealed a task-induced ADC decrease by around 1%. At 3T, the decrease was gradual from stimulus onset and peaked around 8 – 9 s into the paradigm before increasing back to baseline. The return to baseline was complete at the end of the paradigm block in the motor cortex and slower in the visual cortex, up to 8 seconds from the stimulus end. At 7T, the response function in the motor cortex was qualitatively similar to 3T but with a larger amplitude. In the visual cortex, the response was non-monotonic with an initial decrease in ADC, similarly to 3T, followed by a very rapid return to baseline and post-stimulus over-shoot in ADC. These main time-courses are overlaid in **Figure 5** for better comparison. For the other acquisition protocols **(Figure 4**), the qualitative trends of the response functions were similar to BOLD, pointing to the importance of each step in our optimized dfMRI (Column B) to minimize vascular contributions. For example, *b*=0.2 time-courses analyzed independently as a pseudo T_2-BOLD with small diffusion-weighting – likely suppressing the contribution from blood spins – still revealed BOLD-like response due to T_2-weighting, particularly clear in the visual cortex (Column C). Few datasets are available for *b*=0/1 ADC, but they show nonetheless an increase in ADC during task in the visual cortex, similarly to BOLD, but a decrease in the motor cortex (Column D). Finally, the protocol with monopolar diffusion gradient pulses resulted in a nearly flat response in the visual cortex and an increase in ADC in the motor cortex (Column E).

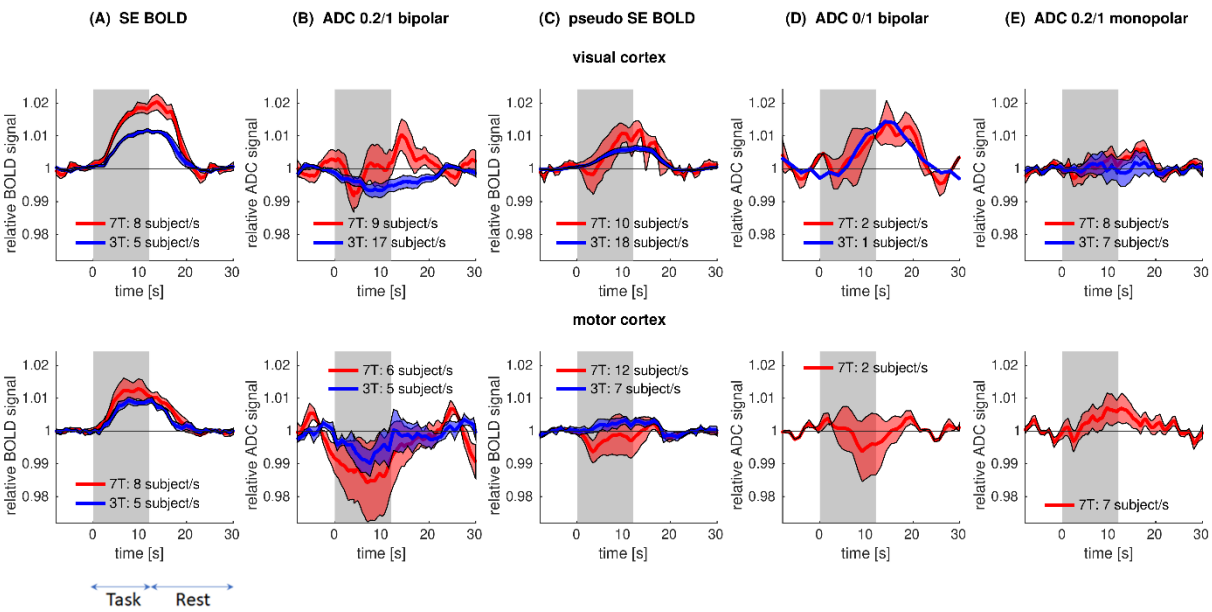

Figure 4. Group-averaged response functions for SE BOLD (A), dfMRI from *b*=0.2/1 pairs bipolar (B), pseudo SE BOLD (C), dfMRI from *b*=0/1 pairs bipolar (D), and dfMRI from *b*=0.2/1 pairs monopolar (E), at 3T and 7T. For each subject, the average time-course of voxels with *z*-statistic > 3.1 in each of the ROIs was first averaged across trials. Subject-level estimates were then normalized to their baseline level and averaged across the cohort. The shaded area represents the standard error of the mean: SEM, calculated across subject-level estimates.

bioRxiv preprint doi: https://doi.org/10.1101/2021.05.16.444253; this version posted May 17, 2021. The copyright holder for this preprint (which was not certified by peer review) is the author/funder, who has granted bioRxiv a license to display the preprint in perpetuity. It is made available under aCC-BY-NC-ND 4.0 International license.

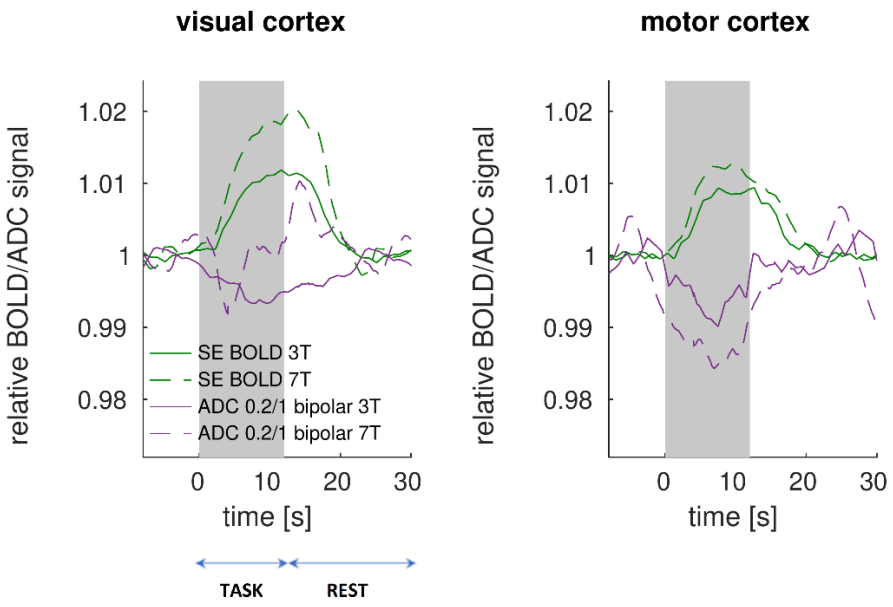

Figure 5. Group average response functions for SE BOLD and dfMRI at 3T and 7T in the visual and motor cortices.

Illustrative examples of individual responses to task for Protocol (2) (ADC *b*=0.2/1 bipolar) are shown in **Supplementary Figure 3**.

Resting-state functional connectivity

Group averages of FC matrices following manual ICA cleaning and GSR were dominated by strong positive correlations, which agreed remarkably well between T_2-BOLD and dfMRI methods, at both field strengths (**Figure 6**). However, our dfMRI protocol attenuated anti-correlations preferentially compared to T_2-BOLD, particularly at 3T. Indeed, the slope of the linear regression of dfMRI to T_2-BOLD positive correlations was 0.93 at 3T and 0.92 at 7T, while for T_2-BOLD negative correlations, the slope dropped to 0.28 at 3T and 0.51 at 7T, respectively. *t*-tests of FC strength between the two protocols showed that the majority of edges with significantly different connectivity had either a low or negative correlation in BOLD, which was further attenuated in dfMRI (**Supplementary Table 1**).

Remarkably, FC patterns were very similar between our dfMRI protocol and the blood-attenuated pseudo SE BOLD (**Supplementary Figure 4**). As in dfMRI, the anti-correlations were reduced in pseudo SE BOLD and both positive and negative correlations agreed between the two methods. It should be underlined that the FC comparison is all the more powerful between these protocols as the underlying data were acquired during the same run, and thus for identical brain activity and physiological conditions in the volunteer.

Finally, the comparison of how various processing steps impact functional connectivity as estimated from the different protocols (SE BOLD, pseudo SE BOLD and ADC 0.2/1 bipolar) suggests that, while ICA cleaning affects SE BOLD connectivity – by removing unwanted physiological artifacts, it has little impact on ADC-derived connectivity (see **Figure 7** for 3T and **Supplementary Figure 5** for 7T). By intrinsically removing large field fluctuation contributions to functional contrast, such as those of vascular origin, ADC dfMRI also has a valuable attribute of yielding data that is *"clean"* by design.

bioRxiv preprint doi: https://doi.org/10.1101/2021.05.16.444253; this version posted May 17, 2021. The copyright holder for this preprint (which was not certified by peer review) is the author/funder, who has granted bioRxiv a license to display the preprint in perpetuity. It is made available under aCC-BY-NC-ND 4.0 International license.

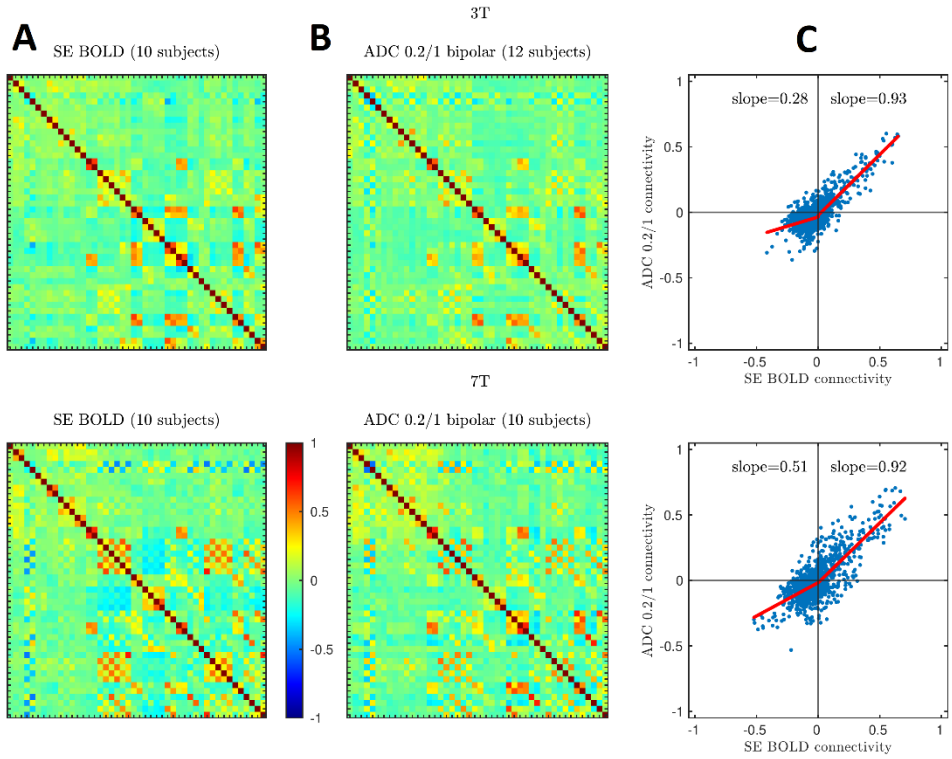

Figure 6. Resting-state analysis following manual ICA cleaning and GSR. Group averages of FC matrices from SE BOLD (**A**) and *b*=0.2/1 ADC (**B**) at 3T and 7T. **C**: Correlation of FC strength derived from SE BOLD vs. dfMRI. The positive edges in BOLD fMRI agree exceptionally well with dfMRI FC (slope of the linear regression ~1 at both field strengths). However, BOLD anti-correlations are largely suppressed in dfMRI, particularly at the lower field.

Discussion

This is the first dfMRI study in humans attempting to minimize BOLD contamination sources and compare functional responses at two field strengths, both for task and resting-state fMRI. Our study further benefits from unprecedented high spatial and temporal resolution of 2 – 2.5 mm isotropic and 1 – 2 s.

Task fMRI

The optimized dfMRI protocol was the only one to yield a consistent decrease in ADC during task, as expected from biophysical mechanisms and previously reported in experiments on tissue samples without vasculature (Flint et al., 2009; Tirosh and Nevo, 2013; Spees et al., 2018). All other *"dfMRI"* protocols yielded BOLD-like response functions (from T_2-weighting or direct blood pool contributions), with a directionality not fully consistent across ROIs or field strengths. This inconsistency (e.g. for ADC time-course from *b*=0/1, between the visual and motor cortices) could be related to spatially varying SNR levels, field homogeneity, magnitude of the neuronal response and of a competing BOLD response. The ADC time-course from *b*=0.2/1 pairs with monopolar gradient pulses showed a weak, nearly flat response at 3T, potentially resulting from competing dfMRI and BOLD mechanisms balancing out the net effect.

bioRxiv preprint doi: https://doi.org/10.1101/2021.05.16.444253; this version posted May 17, 2021. The copyright holder for this preprint (which was not certified by peer review) is the author/funder, who has granted bioRxiv a license to display the preprint in perpetuity. It is made available under aCC-BY-NC-ND 4.0 International license.

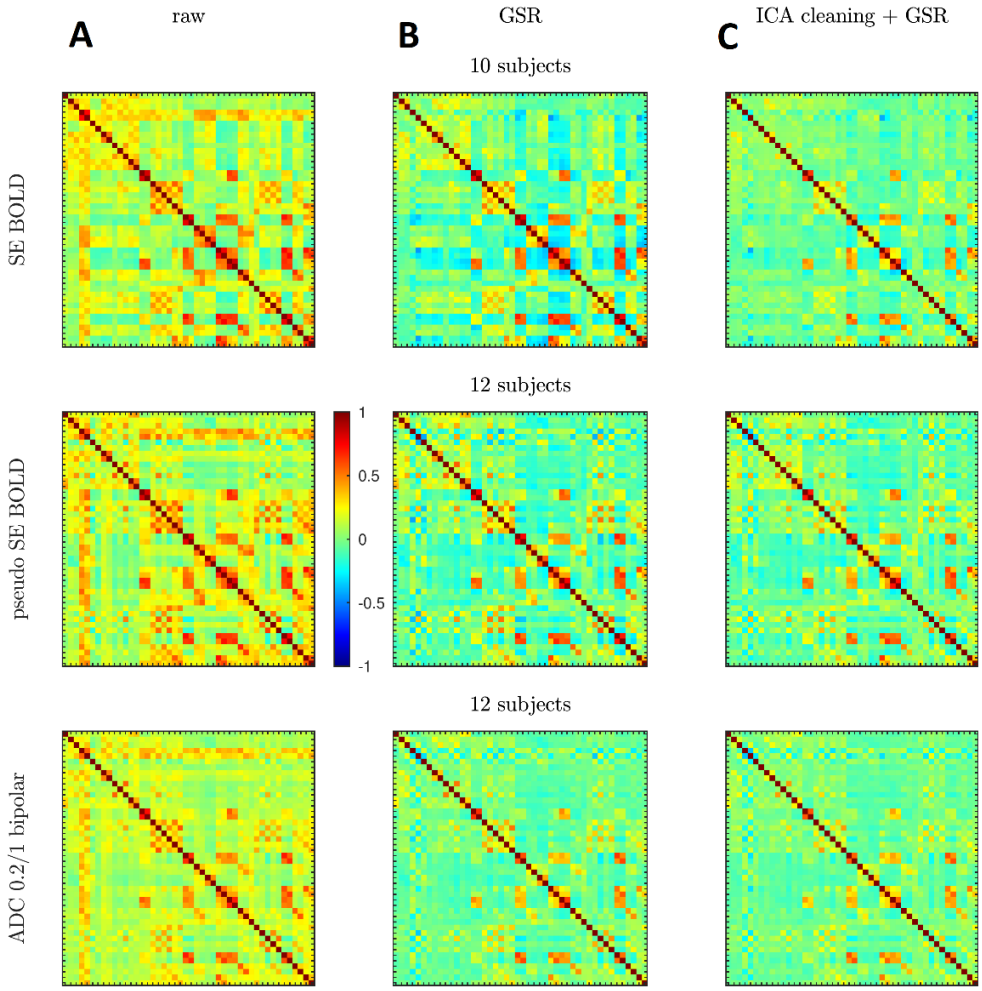

Figure 7. Average functional connectivity matrices at 3T, derived from either *"raw"* signal (A), after GSR (B) or after manual ICA cleaning followed by GSR (C). Rows correspond to RS-FC derived from various protocols: SE BOLD, pseudo SE BOLD (b=0.2 time-courses) and ADC (from pairs b=0.2/1 – Protocol (2)).

A close comparison between T_2-BOLD and *"optimized"* dfMRI characteristics suggests different contrast mechanisms between the two. Indeed, the BOLD response was delayed with respect to the stimulus onset and, once established, the plateau lasted at least until the stimulus end (motor cortex) or beyond (visual cortex) before gradually decreasing to baseline. Return to baseline was reached within eight seconds from the stimulus end. The differences in BOLD response between cortical areas may be due to a difference in stimulus strength and persistency as well as in hemodynamic response (West et al., 2019). In contrast, for both ROIs and at both field strengths, the ADC decrease started upon stimulus onset and time to trough was 8 – 9 seconds into the stimulus. In the motor cortex at 3T, the ADC increased back towards baseline at the end of the stimulus, while the BOLD plateau was maintained beyond. In the visual cortex at 7T, there was a more rapid return of ADC to baseline and a positive overshoot after the stimulus period. The first component might reflect rapid microstructural changes, and the latter slower but notable BOLD contamination, in full agreement with a recent dfMRI study at 9.4T in rats (Nunes et al., 2021).

The difference in dfMRI qualitative trend between 3T and 7T suggests vascular contributions may be more challenging to mitigate at higher fields due to stronger susceptibility, despite a careful sequence design. In the motor cortex, the dfMRI responses were qualitatively more consistent between 3T and 7T, with a gradual decrease initiated without delay from stimulus onset and 8-second time to trough, followed by a gradual return to baseline after stimulus end. BOLD effects may be brain-region

bioRxiv preprint doi: https://doi.org/10.1101/2021.05.16.444253; this version posted May 17, 2021. The copyright holder for this preprint (which was not certified by peer review) is the author/funder, who has granted bioRxiv a license to display the preprint in perpetuity. It is made available under aCC-BY-NC-ND 4.0 International license.

dependent and less pronounced in the motor vs. the visual cortex. It is worth noting, for instance, that BOLD amplitude difference between 7T and 3T was very pronounced in the visual cortex, but not so marked in the motor cortex. However, the magnitude of the dfMRI effect (via the ADC decrease) does appear to be field-dependent also in the motor cortex, whereby vascular contributions to dfMRI cannot be ruled out in this ROI at 7T.

The relatively smooth and persistent ADC decrease during task is consistent with previous dfMRI studies (Darquie et al., 2001; Spees et al., 2018) and also with expected gradual changes in the overall volume of neuronal, glial and extracellular compartments upon sustained firing, as highlighted by the electrodiffusive neuron-extracellular-glia model (Sætra et al., 2020).

We report an amplitude of ADC decrease on the order of 1% in physiological conditions of sensory and motor stimulation. This magnitude of the effect is weak but nonetheless detectable, and sensible when compared to preclinical dfMRI studies using chemical or electrical stimulation above physiological thresholds, and which reported ADC drops of 6 – 50% (Flint et al., 2009; Spees et al., 2018). It is also important to note that our estimated response functions were somewhat noisier than in some of the previous literature, where the time-courses were filtered – either with a median filter (Nunes et al., 2021) or with a moving average filter (Darquie et al., 2001; Luca et al., 2019). We preferred not to use a filter, as a filter could have hidden subtle ADC dynamics.

As for the temporal characteristics, the spatial distribution of activated voxels was also very different between BOLD and dfMRI. As expected, the smaller dfMRI effect size resulted in a more limited activation pattern and weaker statistics at the group level. Nevertheless, the activated voxels consistently followed cortical ribbons in the active areas, yielding more specific information than large BOLD clusters. While cortical layer-specific activation patterns can be achieved with BOLD or VASO fMRI at ultra-high fields while scanning at very high spatial resolution, particularly strikingly with laminar fMRI (Huber et al., 2017), with dfMRI such patterns were accessible using much less demanding settings: a 3T field strength and a spatial resolution of 2.5 mm (which corresponds to the average human cortical thickness). Furthermore, the BOLD cluster peaks did not coincide spatially with dfMRI peaks, suggesting dfMRI contrast is distinct from a residual strong BOLD contamination. We note that our implementation of BOLD corresponded to T_2-BOLD, which has improved sensitivity towards capillaries than the more common T_2*-BOLD, where the largest signals stem from draining veins.

The analysis of the spatial location of active voxels with either method also highlighted a larger proportion of active voxels in major white matter tracts – as labelled in the Johns Hopkins University atlas (Mori, 2005) – with dfMRI (5 – 7%) vs. SE BOLD (1%). It is well established that BOLD sensitivity in white matter is much reduced due to lower blood volume and flow as well as energy requirements compared to gray matter. As a result, most resting-state and some task BOLD fMRI studies still use the white matter signal as a nuisance regressor. Although white matter BOLD is regaining interest (Gore et al., 2019; Grajauskas et al., 2019) – possibly thanks to higher field strengths and spatial resolution boosting sensitivity and specificity – the positive findings in this field remain limited. DfMRI has been singled out as a promising technique to detect white matter activity, and a decrease in ADC upon sustained stimulation was measurable in *ex vivo* nerve sample or mouse optic nerve (Lin et al., 2014; Spees et al., 2018, 2013). Our results support the stronger potential of dfMRI vs. BOLD to detect white matter activity. This potential requires, however, further investigation given the more limited sensitivity of dfMRI overall.

bioRxiv preprint doi: https://doi.org/10.1101/2021.05.16.444253; this version posted May 17, 2021. The copyright holder for this preprint (which was not certified by peer review) is the author/funder, who has granted bioRxiv a license to display the preprint in perpetuity. It is made available under aCC-BY-NC-ND 4.0 International license.

Resting-state functional connectivity

Based on resting-state data that underwent ICA cleaning and GSR, or GSR alone, we found primarily reduced anti-correlations and maintained positive correlations in dfMRI RS-FC vs. BOLD, which supports two hypotheses.

First, that GSR does not result in a plain mathematical demeaning of FC matrices but contributes to highlighting genuine (anti-)correlations across the brain, should they exist. This finding is in agreement with recent studies – both in humans and rodents – showing that ICA cleaning + GSR also improves the differentiation between populations based on resting-state patterns compared to ICA cleaning alone (Li et al., 2019; Diao et al., 2021). While GSR is known to mathematically favor anti-correlations, there is also evidence of genuine anti-correlations in BOLD resting-state functional connectivity, which are reportedly related to certain brain networks being specifically inactivated while other networks are active, for accrued efficiency (Fox et al., 2005), e.g. default-mode vs. executive control networks (Fox et al., 2009; Nalci et al., 2017). Thus, they could have the same vascular origin as negative BOLD, related to arteriolar vasoconstriction and reduced oxygenation in areas of suppressed neuronal firing (Devor et al., 2007; Bianciardi et al., 2011).

Second, and most importantly for our purposes, this difference in RS-FC patterns between BOLD and dfMRI suggests that there is no twin of negative BOLD in dfMRI and that the sources of dfMRI signal are distinct from those of BOLD and largely free of vascular contributions, in agreement with previous findings in the rat brain (Abe et al., 2020; Jelescu, I.O., 2019). Indeed, from the perspective of neuron microstructural fluctuations, inhibitory activity leading to membrane hyperpolarization is not expected to alter the cell volume and/or morphology significantly relative to baseline – i.e. the change in membrane potential between resting and hyperpolarized states is small compared to the dramatic change in membrane potential incurred during firing (Fraser and Huang, 2004).

We note that the pseudo SE BOLD data (based on b=0.2 ms/μm^2 time-courses) yielded RS-FC with attenuated anti-correlations and that agreed remarkably well with dfMRI RS-FC coefficients. Therefore, it would appear that BOLD anti-correlations could be driven by signal contributions from the blood pool, which are already largely attenuated using mild diffusion-weighting.

Finally, while ICA cleaning had a significant impact on BOLD RS-FC, the effect was lesser on dfMRI RS-FC. This is consistent with the fact that ICA components typically identified as artifacts are largely of physiological origin, be it variations in heart rate, breathing rate, or motion that affect the field homogeneity and contribute to non-BOLD T_2(*) fluctuations. From this perspective, dfMRI time-courses can be considered *"self-cleaned"*, which represents a major advantage in limiting pre-processing steps and reducing within- and between-subject confounding variability.

Limitations

In the interest of temporal resolution, this study used a short TR of 1 s, atypical for multi-slice SE-EPI and which only allowed limited T_1 recovery – especially at 7T – resulting in limited SNR. Furthermore, the B_1 transmit field inhomogeneity is notoriously pronounced at high field, further causing signal loss for a spin-echo and all the more for a double spin-echo sequence design. The relatively low SNR was, however, mitigated by the MP-PCA denoising approach.

The relatively high temporal resolution also prevented whole-brain coverage. Thus, the analysis of dfMRI responses was confined to a slab covering the areas anticipated as most relevant for either task or resting-state. However, the achievable brain coverage was doubled using multiband acceleration of factor 2, with some further penalty in SNR. Additional brain regions may be of interest, particularly

bioRxiv preprint doi: https://doi.org/10.1101/2021.05.16.444253; this version posted May 17, 2021. The copyright holder for this preprint (which was not certified by peer review) is the author/funder, who has granted bioRxiv a license to display the preprint in perpetuity. It is made available under aCC-BY-NC-ND 4.0 International license.

given the spatial mismatch between BOLD and dfMRI cluster peaks (i.e. voxels with the strongest activation in either case) and between RS-FC patterns. Overall, our acquisition protocol achieved a sensible trade-off between temporal resolution, spatial resolution, SNR and brain coverage. Still, ongoing efforts in acquisition strategies, acceleration and efficiency may allow to further optimize these parameters concomitantly.

Both the task and resting-state results showed that the dfMRI signal at 7T shared combined features of dfMRI at 3T and BOLD. This suggests that despite a careful experimental design, vascular contributions to dfMRI cannot be suppressed entirely, especially at higher field strengths, where susceptibility effects are more pronounced.

All of the above limitations point towards dfMRI being perhaps better suited for lower field strengths. Interestingly, now in the MRI community, there is an increasing interest in low-field systems (Campbell-Washburn et al., 2019; Wang et al., 2021). While lower fields are detrimental to SNR and CNR in BOLD fMRI, and laminar fMRI in particular, for dfMRI, low-fields may yield acceptable SNR (via shorter T_1 and more homogeneous B_1), larger brain coverage (via reduced radio-frequency power deposition and heating) and cleaner, more specific contrast (via reduced BOLD contributions).

One potential indirect BOLD contribution that our protocol did not account for is a decrease in CSF volume as a compensation mechanism for an increase in blood volume during the hemodynamic response (Jin and Kim, 2010; Thomas et al., 2013). However, diffusion-weighting is expected to also attenuate the contribution from the fast-diffusing CSF compartment quite substantially, reducing the impact of this effect. Future dfMRI protocols could nonetheless include an initial CSF-nulling inversion pulse (Chou et al., 2005) to address this confound directly.

Conclusions

Taken together, our task and resting-state results support the existence and detectability of genuine dfMRI contrast distinct from BOLD mechanisms, made possible by a careful study design to minimize vascular contributions. DfMRI enables a more specific detection of activation in response to task and resting-state functional connectivity mapping directly free from physiological artifacts. Finally, dfMRI is ideally suited for low or intermediate magnetic field systems. This will become an important asset in the context of increasing interest for low-field systems, and provide a unique functional MRI technique in a context where BOLD may lack sensitivity.

Acknowledgements

We would like to thank Dimitri Van De Ville, Essa Yacoub, Eleonora Fornari, Lijing Xin, Olivier Reynaud and Jelle Veraart for much valuable advice and very helpful discussions. This work was supported by the Swiss National Science Foundation under a Spark award 190882 (to I.O.J.). We are grateful for the provision of simultaneous multi-slice (multiband) pulse sequence and reconstruction algorithms from the Center for Magnetic Resonance Research, University of Minnesota. We acknowledge access to the facilities and expertise of the CIBM Center for Biomedical Imaging, a Swiss research center of excellence founded and supported by Lausanne University Hospital (CHUV), University of Lausanne (UNIL), Ecole polytechnique fédérale de Lausanne (EPFL), University of Geneva (UNIGE) and Geneva University Hospitals (HUG).

bioRxiv preprint doi: https://doi.org/10.1101/2021.05.16.444253; this version posted May 17, 2021. The copyright holder for this preprint (which was not certified by peer review) is the author/funder, who has granted bioRxiv a license to display the preprint in perpetuity. It is made available under aCC-BY-NC-ND 4.0 International license.

References

Abe, Y., Takata, N., Sakai, Y., Hamada, H.T., Hiraoka, Y., Aida, T., Tanaka, K., Bihan, D.L., Doya, K., Tanaka, K.F., 2020. Diffusion functional MRI reveals global brain network functional abnormalities driven by targeted local activity in a neuropsychiatric disease mouse model. NeuroImage 223, 117318. https://doi.org/10.1016/j.neuroimage.2020.117318

Abe, Y., Tsurugizawa, T., Le Bihan, D., 2017. Water diffusion closely reveals neural activity status in rat brain loci affected by anesthesia. PLOS Biol. 15, e2001494. https://doi.org/10.1371/journal.pbio.2001494

Ades-Aron, B., Lemberskiy, G., Veraart, J., Golfinos, J., Fieremans, E., Novikov, D.S., Shepherd, T., 2021. Improved Task-based Functional MRI Language Mapping in Patients with Brain Tumors through Marchenko-Pastur Principal Component Analysis Denoising. Radiology 298, 365–373. https://doi.org/10.1148/radiol.2020200822

Alfaro-Almagro, F., Jenkinson, M., Bangerter, N.K., Andersson, J.L.R., Griffanti, L., Douaud, G., Sotiropoulos, S.N., Jbabdi, S., Hernandez-Fernandez, M., Vallee, E., Vidaurre, D., Webster, M., McCarthy, P., Rorden, C., Daducci, A., Alexander, D.C., Zhang, H., Dragonu, I., Matthews, P.M., Miller, K.L., Smith, S.M., 2018. Image processing and Quality Control for the first 10,000 brain imaging datasets from UK Biobank. NeuroImage 166, 400–424. https://doi.org/10.1016/j.neuroimage.2017.10.034

Andersson, J.L.R., Skare, S., Ashburner, J., 2003. How to correct susceptibility distortions in spin-echo echo-planar images: application to diffusion tensor imaging. NeuroImage 20, 870–888. https://doi.org/10.1016/S1053-8119(03)00336-7

Andrew, R.D., Macvicar, B.A., 1994. Imaging cell volume changes and neuronal excitation in the hippocampal slice. Neuroscience 62, 371–383. https://doi.org/10.1016/0306-4522(94)90372-7

Autio, J.A.A., Kershaw, J., Shibata, S., Obata, T., Kanno, I., Aoki, I., 2011. High b-value diffusion-weighted fMRI in a rat forepaw electrostimulation model at 7 T. Neuroimage 57, 140–148. https://doi.org/10.1016/j.neuroimage.2011.04.006

Avants, B.B., Tustison, N.J., Song, G., Cook, P.A., Klein, A., Gee, J.C., 2011. A reproducible evaluation of ANTs similarity metric performance in brain image registration. NeuroImage 54, 2033–2044. https://doi.org/10.1016/j.neuroimage.2010.09.025

Avants, B.B., Yushkevich, P., Pluta, J., Minkoff, D., Korczykowski, M., Detre, J., Gee, J.C., 2010. The optimal template effect in hippocampus studies of diseased populations. NeuroImage 49, 2457–2466. https://doi.org/10.1016/j.neuroimage.2009.09.062

Bai, R., Stewart, C.V., Plenz, D., Basser, P.J., 2016. Assessing the sensitivity of diffusion MRI to detect neuronal activity directly. Proc. Natl. Acad. Sci. 113, E1728–E1737. https://doi.org/10.1073/pnas.1519890113

Beckmann, C.F., Smith, S.M., 2004. Probabilistic Independent Component Analysis for Functional Magnetic Resonance Imaging. IEEE Trans. Med. Imaging 23, 137–152. https://doi.org/10.1109/TMI.2003.822821

Bianciardi, M., Fukunaga, M., van Gelderen, P., de Zwart, J.A., Duyn, J.H., 2011. Negative BOLD-fMRI Signals in Large Cerebral Veins. J. Cereb. Blood Flow Metab. 31, 401–412. https://doi.org/10.1038/jcbfm.2010.164

Campbell-Washburn, A.E., Ramasawmy, R., Restivo, M.C., Bhattacharya, I., Basar, B., Herzka, D.A., Hansen, M.S., Rogers, T., Bandettini, W.P., McGuirt, D.R., Mancini, C., Grodzki, D., Schneider, R., Majeed, W., Bhat, H., Xue, H., Moss, J., Malayeri, A.A., Jones, E.C., Koretsky, A.P., Kellman, P., Chen, M.Y., Lederman, R.J., Balaban, R.S., 2019. Opportunities in Interventional and Diagnostic Imaging by Using High-Performance Low-Field-Strength MRI. Radiology 293, 384–393. https://doi.org/10.1148/radiol.2019190452

Caprio, M., Russo, C., Giugliano, A., Ragucci, M., Mancini, M., 2016. Vascular disease in patients with multiple sclerosis: a review. J Vasc Med Surg 4, 746–753.

Chou, M.-C., Lin, Y.-R., Huang, T.-Y., Wang, C.-Y., Chung, H.-W., Juan, C.-J., Chen, C.-Y., 2005. FLAIR diffusion-tensor MR tractography: comparison of fiber tracking with conventional imaging. AJNR Am. J. Neuroradiol. 26, 591–597.

bioRxiv preprint doi: https://doi.org/10.1101/2021.05.16.444253; this version posted May 17, 2021. The copyright holder for this preprint (which was not certified by peer review) is the author/funder, who has granted bioRxiv a license to display the preprint in perpetuity. It is made available under aCC-BY-NC-ND 4.0 International license.

Darquie, A., Poline, J.B., Poupon, C., Saint-Jalmes, H., Le Bihan, D., 2001. Transient decrease in water diffusion observed in human occipital cortex during visual stimulation. Proc Natl Acad Sci U A 98, 9391–5. https://doi.org/10.1073/pnas.151125698

Devor, A., Tian, P., Nishimura, N., Teng, I.C., Hillman, E.M.C., Narayanan, S.N., Ulbert, I., Boas, D.A., Kleinfeld, D., Dale, A.M., 2007. Suppressed Neuronal Activity and Concurrent Arteriolar Vasoconstriction May Explain Negative Blood Oxygenation Level-Dependent Signal. J. Neurosci. 27, 4452–4459. https://doi.org/10.1523/JNEUROSCI.0134-07.2007

Diao, Y., Yin, T., Gruetter, R., Jelescu, I.O., 2021. PIRACY: An Optimized Pipeline for Functional Connectivity Analysis in the Rat Brain. Front. Neurosci. 15, 602170. https://doi.org/10.3389/fnins.2021.602170

Dubois, J., Adolphs, R., 2016. Building a Science of Individual Differences from fMRI. Trends Cogn. Sci. 20, 425–443. https://doi.org/10.1016/j.tics.2016.03.014

Flint, J., Hansen, B., Vestergaard-Poulsen, P., Blackband, S.J., 2009. Diffusion weighted magnetic resonance imaging of neuronal activity in the hippocampal slice model. Neuroimage 46, 411–8. https://doi.org/10.1016/j.neuroimage.2009.02.003

Fox, M.D., Snyder, A.Z., Vincent, J.L., Corbetta, M., Van Essen, D.C., Raichle, M.E., 2005. The human brain is intrinsically organized into dynamic, anticorrelated functional networks. Proc. Natl. Acad. Sci. U. S. A. 102, 9673. https://doi.org/10.1073/pnas.0504136102

Fox, M.D., Zhang, D., Snyder, A.Z., Raichle, M.E., 2009. The global signal and observed anticorrelated resting state brain networks. J Neurophysiol 101, 3270–83. https://doi.org/10.1152/jn.90777.2008

Fraser, J.A., Huang, C.L.-H., 2004. A quantitative analysis of cell volume and resting potential determination and regulation in excitable cells. J. Physiol. 559, 459–478. https://doi.org/10.1113/jphysiol.2004.065706

Friston, Karl.J., Ashburner, J., Frith, C.D., Poline, J.-B., Heather, J.D., Frackowiak, R.S.J., 1995. Spatial registration and normalization of images. Hum. Brain Mapp. 3, 165–189. https://doi.org/10.1002/hbm.460030303

Friston, K.J. (Ed.), 2007. Statistical parametric mapping: the analysis of funtional brain images, 1st ed. ed. Elsevier/Academic Press, Amsterdam ; Boston.

Gore, J.C., Li, M., Gao, Y., Wu, T.-L., Schilling, K.G., Huang, Y., Mishra, A., Newton, A.T., Rogers, B.P., Chen, L.M., Anderson, A.W., Ding, Z., 2019. Functional MRI and resting state connectivity in white matter - a mini-review. Magn. Reson. Imaging 63, 1–11. https://doi.org/10.1016/j.mri.2019.07.017

Grajauskas, L.A., Frizzell, T., Song, X., D'Arcy, R.C.N., 2019. White Matter fMRI Activation Cannot Be Treated as a Nuisance Regressor: Overcoming a Historical Blind Spot. Front. Neurosci. 13. https://doi.org/10.3389/fnins.2019.01024

Griffanti, L., Douaud, G., Bijsterbosch, J., Evangelisti, S., Alfaro-Almagro, F., Glasser, M.F., Duff, E.P., Fitzgibbon, S., Westphal, R., Carone, D., Beckmann, C.F., Smith, S.M., 2017. Hand classification of fMRI ICA noise components. NeuroImage 154, 188–205. https://doi.org/10.1016/j.neuroimage.2016.12.036

Henson, R., Rugg, M.D., Friston, K.J., 2001. The choice of basis functions in event-related fMRI. NeuroImage 13, 149. https://doi.org/10.1016/S1053-8119(01)91492-2

Huber, L., Handwerker, D.A., Jangraw, D.C., Chen, G., Hall, A., Stüber, C., Gonzalez-Castillo, J., Ivanov, D., Marrett, S., Guidi, M., Goense, J., Poser, B.A., Bandettini, P.A., 2017. High-Resolution CBV-fMRI Allows Mapping of Laminar Activity and Connectivity of Cortical Input and Output in Human M1. Neuron 96, 1253-1263.e7. https://doi.org/10.1016/j.neuron.2017.11.005

Jelescu, I.O., 2019. Resting-state diffusion fMRI bears strong resemblance and only subtle differences to BOLD fMRI. ISMRM.

Jenkinson, M., Beckmann, C.F., Behrens, T.E.J., Woolrich, M.W., Smith, S.M., 2012. FSL. NeuroImage 62, 782–790. https://doi.org/10.1016/j.neuroimage.2011.09.015

Jin, T., Kim, S.-G., 2010. Change of the cerebrospinal fluid volume during brain activation investigated by T1ρ-weighted fMRI. NeuroImage 51, 1378–1383. https://doi.org/10.1016/j.neuroimage.2010.03.047

bioRxiv preprint doi: https://doi.org/10.1101/2021.05.16.444253; this version posted May 17, 2021. The copyright holder for this preprint (which was not certified by peer review) is the author/funder, who has granted bioRxiv a license to display the preprint in perpetuity. It is made available under aCC-BY-NC-ND 4.0 International license.

Jin, T., Kim, S.-G., 2008. Functional changes of apparent diffusion coefficient during visual stimulation investigated by diffusion-weighted gradient-echo fMRI. NeuroImage 41, 801–812. https://doi.org/10.1016/j.neuroimage.2008.03.014

Kellner, E., Dhital, B., Kiselev, V.G., Reisert, M., 2016. Gibbs-ringing artifact removal based on local subvoxel-shifts: Gibbs-Ringing Artifact Removal. Magn. Reson. Med. 76, 1574–1581. https://doi.org/10.1002/mrm.26054

Lang, F., Busch, G.L., Ritter, M., Völkl, H., Waldegger, S., Gulbins, E., Häussinger, D., 1998. Functional Significance of Cell Volume Regulatory Mechanisms. Physiol. Rev. 78, 247–306. https://doi.org/10.1152/physrev.1998.78.1.247

Le Bihan, D., Urayama, S., Aso, T., Hanakawa, T., Fukuyama, H., 2006. Direct and fast detection of neuronal activation in the human brain with diffusion MRI. Proc. Natl. Acad. Sci. 103, 8263. https://doi.org/10.1073/pnas.0600644103

Li, J., Kong, R., Liégeois, R., Orban, C., Tan, Y., Sun, N., Holmes, A.J., Sabuncu, M.R., Ge, T., Yeo, B.T.T., 2019. Global signal regression strengthens association between resting-state functional connectivity and behavior. NeuroImage 196, 126–141. https://doi.org/10.1016/j.neuroimage.2019.04.016

Lin, T.-H., Spees, W.M., Chiang, C.-W., Trinkaus, K., Cross, A.H., Song, S.-K., 2014. Diffusion fMRI detects white-matter dysfunction in mice with acute optic neuritis. Neurobiol. Dis. 67, 1–8. https://doi.org/10.1016/j.nbd.2014.02.007

Luca, A.D., Schlaffke, L., Siero, J.C.W., Froeling, M., Leemans, A., 2019. On the sensitivity of the diffusion MRI signal to brain activity in response to a motor cortex paradigm. Hum. Brain Mapp. 40, 5069–5082. https://doi.org/10.1002/hbm.24758

Miller, K.L., Bulte, D.P., Devlin, H., Robson, M.D., Wise, R.G., Woolrich, M.W., Jezzard, P., Behrens, T.E.J., 2007. Evidence for a vascular contribution to diffusion FMRI at high b value. Proc. Natl. Acad. Sci. 104, 20967–20972. https://doi.org/10.1073/pnas.0707257105

Mori, S. (Ed.), 2005. MRI atlas of human white matter, 1. ed. ed. Elsevier, Amsterdam.

Nalci, A., Rao, B.D., Liu, T.T., 2017. Global signal regression acts as a temporal downweighting process in resting-state fMRI. NeuroImage 152, 602–618. https://doi.org/10.1016/j.neuroimage.2017.01.015

Nunes, D., Gil, R., Shemesh, N., 2021. A rapid-onset diffusion functional MRI signal reflects neuromorphological coupling dynamics. NeuroImage 117862. https://doi.org/10.1016/j.neuroimage.2021.117862

Nunes, D., Ianus, A., Shemesh, N., 2019. Layer-specific connectivity revealed by diffusion-weighted functional MRI in the rat thalamocortical pathway. NeuroImage 184, 646–657. https://doi.org/10.1016/j.neuroimage.2018.09.050

Ogawa, S., Tank, D.W., Menon, R., Ellermann, J.M., Kim, S.G., Merkle, H., Ugurbil, K., 1992. Intrinsic signal changes accompanying sensory stimulation: functional brain mapping with magnetic resonance imaging. Proc Natl Acad Sci U A 89, 5951–5.

Pak, R.W., Hadjiabadi, D.H., Senarathna, J., Agarwal, S., Thakor, N.V., Pillai, J.J., Pathak, A.P., 2017. Implications of neurovascular uncoupling in functional magnetic resonance imaging (fMRI) of brain tumors. J. Cereb. Blood Flow Metab. Off. J. Int. Soc. Cereb. Blood Flow Metab. 37, 3475–3487. https://doi.org/10.1177/0271678X17707398

Peirce, J., Gray, J.R., Simpson, S., MacAskill, M., Höchenberger, R., Sogo, H., Kastman, E., Lindeløv, J.K., 2019. PsychoPy2: Experiments in behavior made easy. Behav. Res. Methods 51, 195–203. https://doi.org/10.3758/s13428-018-01193-y

Polimeni, J.R., Renvall, V., Zaretskaya, N., Fischl, B., 2018. Analysis strategies for high-resolution UHF-fMRI data. NeuroImage 168, 296–320. https://doi.org/10.1016/j.neuroimage.2017.04.053

Raichle, M.E., MacLeod, A.M., Snyder, A.Z., Powers, W.J., Gusnard, D.A., Shulman, G.L., 2001. A default mode of brain function. Proc. Natl. Acad. Sci. 98, 676–682. https://doi.org/10.1073/pnas.98.2.676

Sætra, M.J., Einevoll, G.T., Halnes, G., 2020. An electrodiffusive neuron-extracellular-glia model with somatodendritic interactions. bioRxiv 2020.07.13.200287. https://doi.org/10.1101/2020.07.13.200287

bioRxiv preprint doi: https://doi.org/10.1101/2021.05.16.444253; this version posted May 17, 2021. The copyright holder for this preprint (which was not certified by peer review) is the author/funder, who has granted bioRxiv a license to display the preprint in perpetuity. It is made available under aCC-BY-NC-ND 4.0 International license.

Sherpa, A.D., Xiao, F., Joseph, N., Aoki, C., Hrabetova, S., 2016. Activation of beta-adrenergic receptors in rat visual cortex expands astrocytic processes and reduces extracellular space volume. Synapse 70, 307–16. https://doi.org/10.1002/syn.21908

Shmuel, A., Yacoub, E., Chaimow, D., Logothetis, N.K., Ugurbil, K., 2007. Spatio-temporal point-spread function of fMRI signal in human gray matter at 7 Tesla. NeuroImage 35, 539–552. https://doi.org/10.1016/j.neuroimage.2006.12.030

Spees, W.M., Lin, T.-H., Song, S.-K., 2013. White-matter diffusion fMRI of mouse optic nerve. NeuroImage 65, 209–215. https://doi.org/10.1016/j.neuroimage.2012.10.021

Spees, W.M., Lin, T.H., Sun, P., Song, C., George, A., Gary, S.E., Yang, H.C., Song, S.K., 2018. MRI-based assessment of function and dysfunction in myelinated axons. Proc Natl Acad Sci U A 115, E10225–E10234. https://doi.org/10.1073/pnas.1801788115

Thomas, B.P., Liu, P., Aslan, S., King, K.S., van Osch, M.J.P., Lu, H., 2013. Physiologic underpinnings of negative BOLD cerebrovascular reactivity in brain ventricles. NeuroImage 83, 505–512. https://doi.org/10.1016/j.neuroimage.2013.07.005

Tirosh, N., Nevo, U., 2013. Neuronal activity significantly reduces water displacement: DWI of a vital rat spinal cord with no hemodynamic effect. NeuroImage 76, 98–107. https://doi.org/10.1016/j.neuroimage.2013.02.065

Tsurugizawa, T., Ciobanu, L., Le Bihan, D., 2013. Water diffusion in brain cortex closely tracks underlying neuronal activity. Proc. Natl. Acad. Sci. 110, 11636. https://doi.org/10.1073/pnas.1303178110

Turner, R., 2016. Uses, misuses, new uses and fundamental limitations of magnetic resonance imaging in cognitive science. Philos. Trans. R. Soc. B Biol. Sci. 371, 20150349. https://doi.org/10.1098/rstb.2015.0349

Uğurbil, K., Xu, J., Auerbach, E.J., Moeller, S., Vu, A.T., Duarte-Carvajalino, J.M., Lenglet, C., Wu, X., Schmitter, S., Van de Moortele, P.F., Strupp, J., Sapiro, G., De Martino, F., Wang, D., Harel, N., Garwood, M., Chen, L., Feinberg, D.A., Smith, S.M., Miller, K.L., Sotiropoulos, S.N., Jbabdi, S., Andersson, J.L.R., Behrens, T.E.J., Glasser, M.F., Van Essen, D.C., Yacoub, E., 2013. Pushing spatial and temporal resolution for functional and diffusion MRI in the Human Connectome Project. NeuroImage 80, 80–104. https://doi.org/10.1016/j.neuroimage.2013.05.012

Veraart, J., Novikov, D.S., Christiaens, D., Ades-aron, B., Sijbers, J., Fieremans, E., 2016. Denoising of diffusion MRI using random matrix theory. NeuroImage 142, 394–406. https://doi.org/10.1016/j.neuroimage.2016.08.016

Wang, Y., Gelderen, P., Zwart, J.A., Campbell-Washburn, A.E., Duyn, J.H., 2021. FMRI based on transition-band balanced SSFP in comparison with EPI on a high-performance 0.55 T scanner. Magn. Reson. Med. 85, 3196–3210. https://doi.org/10.1002/mrm.28657

West, K.L., Zuppichini, M.D., Turner, M.P., Sivakolundu, D.K., Zhao, Y., Abdelkarim, D., Spence, J.S., Rypma, B., 2019. BOLD hemodynamic response function changes significantly with healthy aging. NeuroImage 188, 198–207. https://doi.org/10.1016/j.neuroimage.2018.12.012

bioRxiv preprint doi: https://doi.org/10.1101/2021.05.16.444253; this version posted May 17, 2021. The copyright holder for this preprint (which was not certified by peer review) is the author/funder, who has granted bioRxiv a license to display the preprint in perpetuity. It is made available under aCC-BY-NC-ND 4.0 International license.

SUPPLEMENT

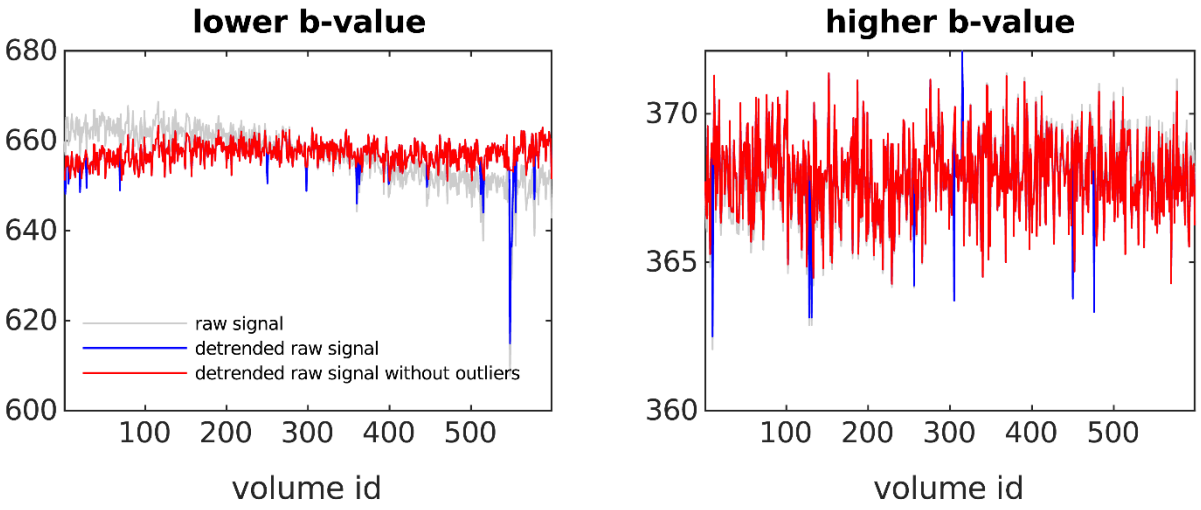

Supplementary Figure 1. Outlier detection and removal for an exemplary dataset. For each volume, the mean across the volume was calculated (gray line). As low-frequency drifts could affect the detection of volume outliers, the signal was then linearly detrended (blue line). A volume was considered an outlier if its detrended average signal was away from the median across all the volumes by more than a pre-specified fraction of this median. This threshold fraction was set at 1% and 3% for 3T and 7T, respectively. Finally, the signal for outliers was replaced with linear interpolation (red line).

bioRxiv preprint doi: https://doi.org/10.1101/2021.05.16.444253; this version posted May 17, 2021. The copyright holder for this preprint (which was not certified by peer review) is the author/funder, who has granted bioRxiv a license to display the preprint in perpetuity. It is made available under aCC-BY-NC-ND 4.0 International license.

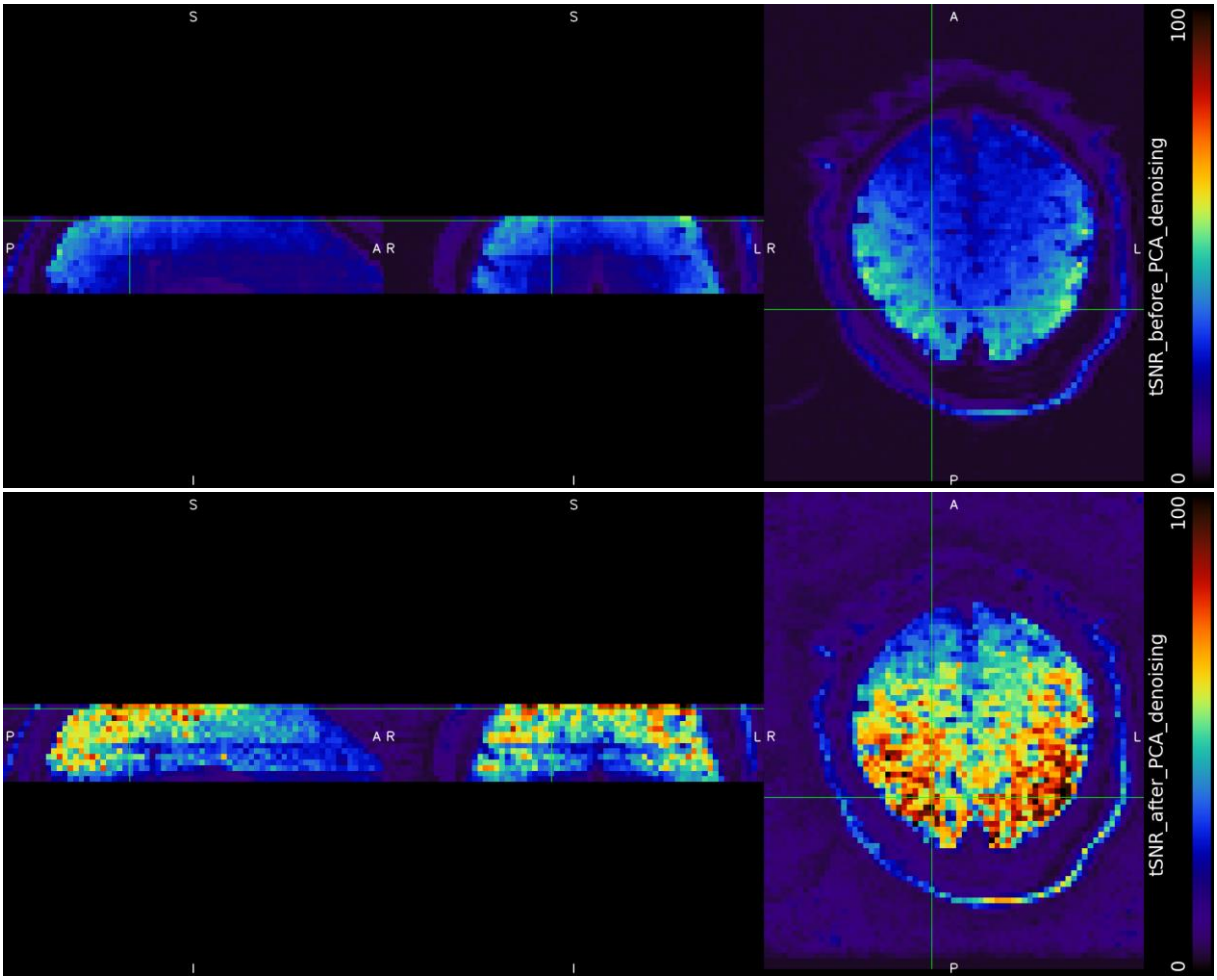

Supplementary Figure 2. tSNR maps before (top panel) and after (bottom panel) MP-PCA denoising for *b*=0.2 volumes of an exemplary subject. The denoising improved tSNR by a factor of almost two.

bioRxiv preprint doi: https://doi.org/10.1101/2021.05.16.444253; this version posted May 17, 2021. The copyright holder for this preprint (which was not certified by peer review) is the author/funder, who has granted bioRxiv a license to display the preprint in perpetuity. It is made available under aCC-BY-NC-ND 4.0 International license.

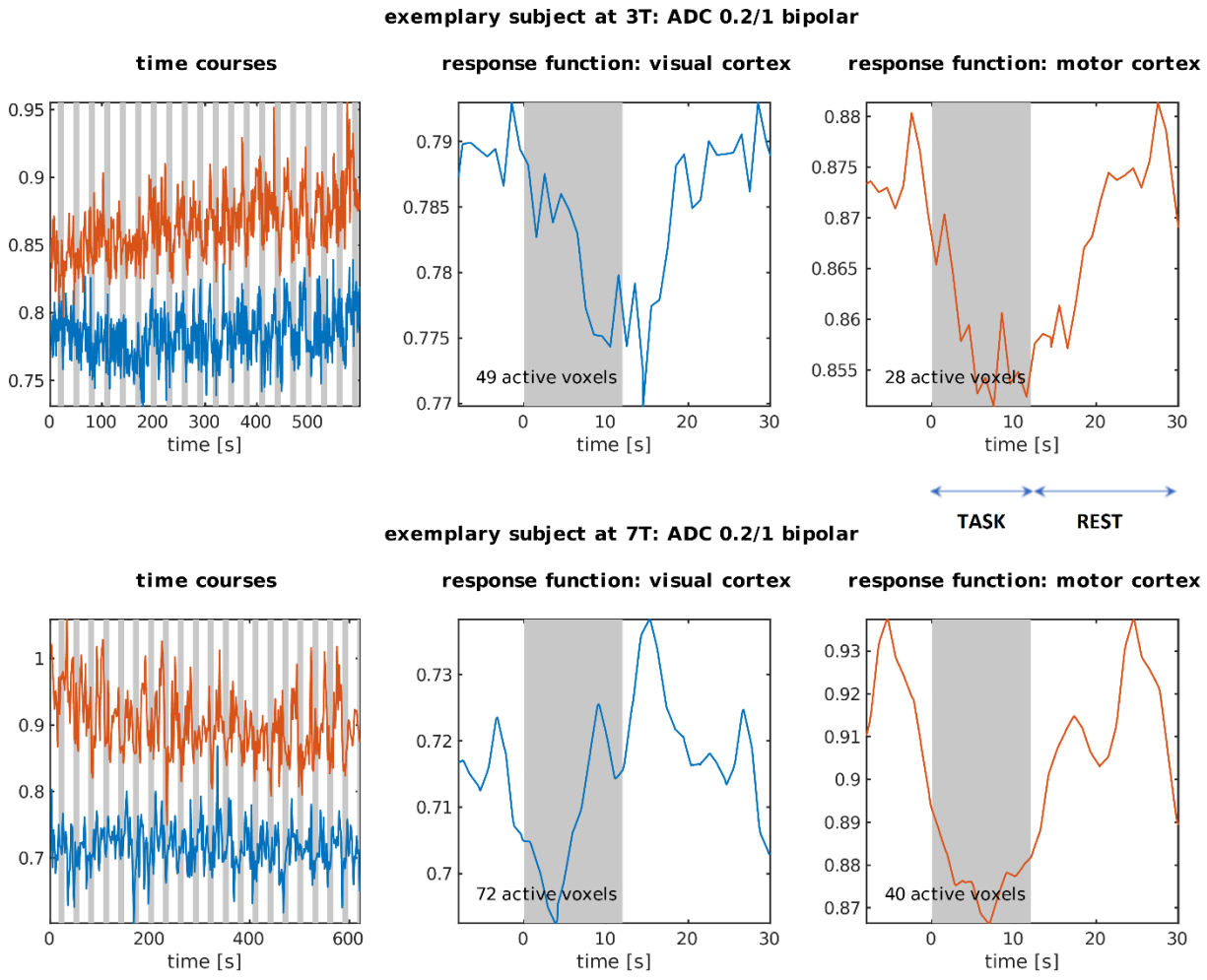

Supplementary Figure 3. Average ADC time-courses and response functions of active voxels (z-statistic > 3.1) in the visual and motor cortices for an individual subject, at 3T (top) and 7T (bottom). The individual response characteristics mirror the group-level analysis and demonstrate a dfMRI response can be recorded at the single-subject level in physiological conditions.

bioRxiv preprint doi: https://doi.org/10.1101/2021.05.16.444253; this version posted May 17, 2021. The copyright holder for this preprint (which was not certified by peer review) is the author/funder, who has granted bioRxiv a license to display the preprint in perpetuity. It is made available under aCC-BY-NC-ND 4.0 International license.

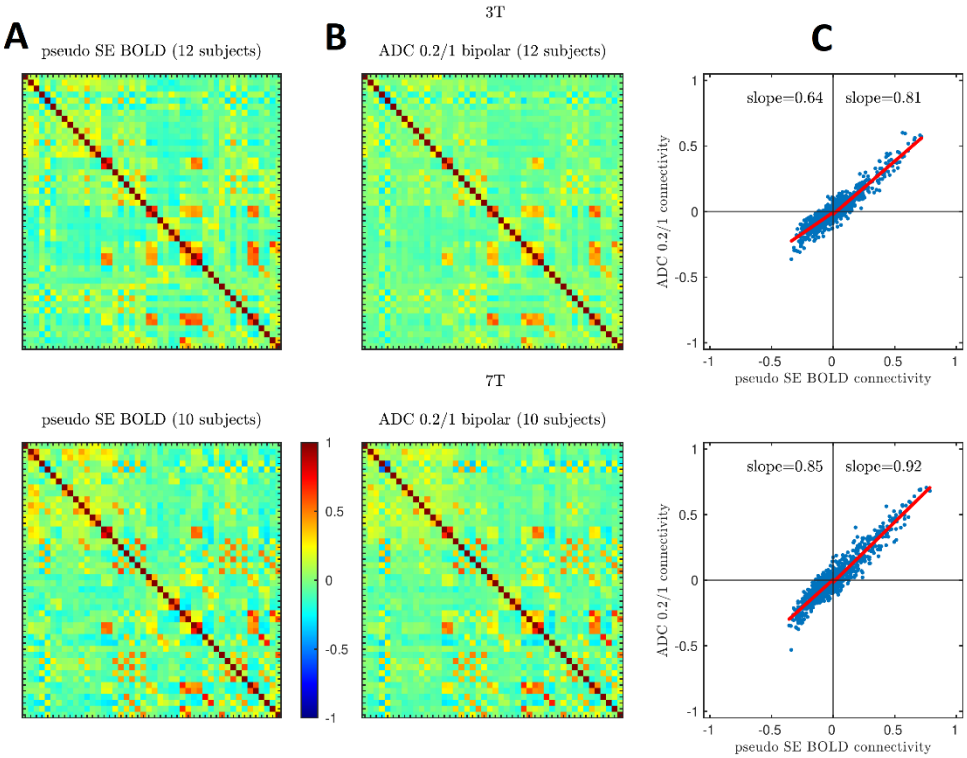

Supplementary Figure 4. Resting-state analysis following manual ICA cleaning and GSR. Group averages of FC matrices from pseudo SE BOLD (**A**) and *b*=0.2/1 ADC (**B**) at 3T and 7T. **C**: Correlation of FC strength derived from pseudo SE BOLD vs. dfMRI. FC coefficients derived from both methods agree more strongly than BOLD vs. dfMRI (**Figure 6**), including negative correlations.

bioRxiv preprint doi: https://doi.org/10.1101/2021.05.16.444253; this version posted May 17, 2021. The copyright holder for this preprint (which was not certified by peer review) is the author/funder, who has granted bioRxiv a license to display the preprint in perpetuity. It is made available under aCC-BY-NC-ND 4.0 International license.

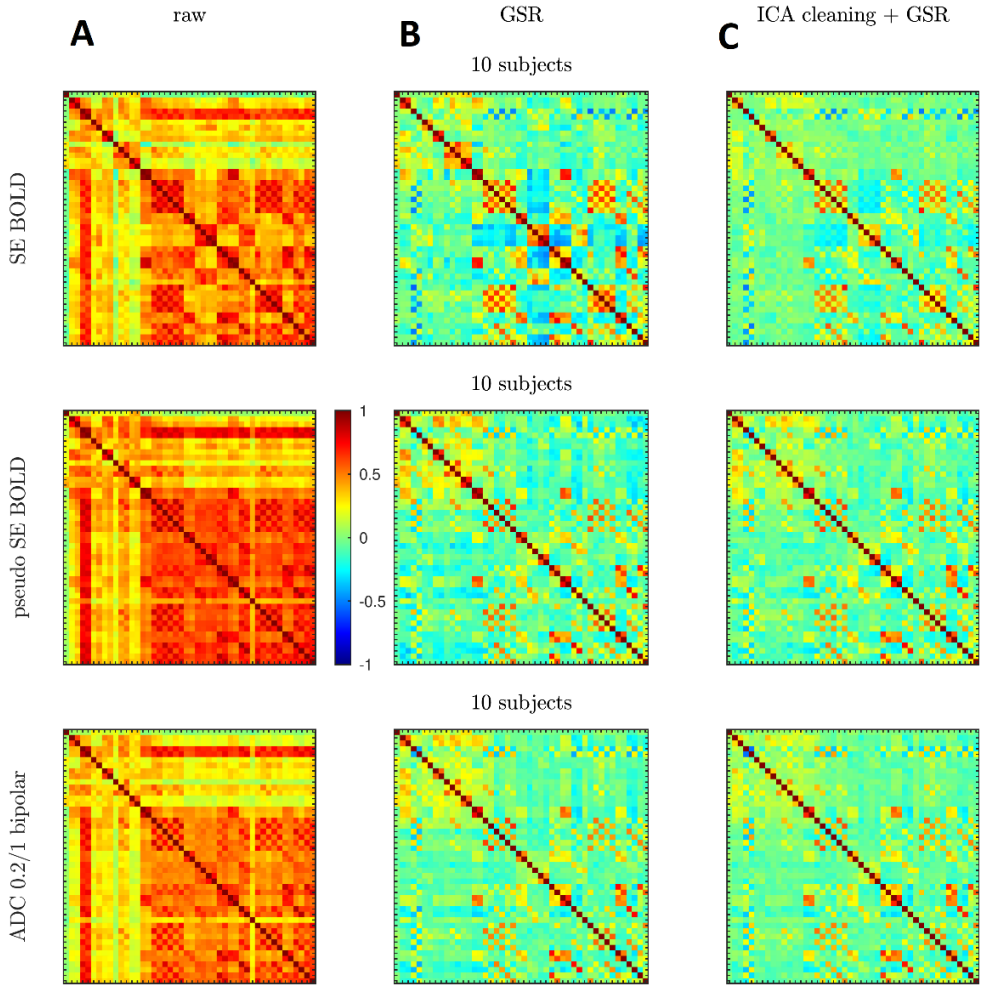

Supplementary Figure 5. Average functional connectivity matrices at 7T, derived from either *"raw"* signal (A), after GSR (B) or after manual ICA cleaning followed by GSR (C). Rows correspond to RS-FC derived from various protocols: SE BOLD, pseudo SE BOLD (*b*=0.2 time-courses) and ADC (from pairs *b*=0.2/1 – Protocol (2)).

bioRxiv preprint doi: https://doi.org/10.1101/2021.05.16.444253; this version posted May 17, 2021. The copyright holder for this preprint (which was not certified by peer review) is the author/funder, who has granted bioRxiv a license to display the preprint in perpetuity. It is made available under aCC-BY-NC-ND 4.0 International license.

Supplementary Table 1. Resting-state functional connectivity edges with most significant differences between SE BOLD and ADC *b*=0.2/1 bipolar, dependent on the field strength, following GSR without manual ICA cleaning. ROIs come from the Neuromorphometrics atlas. The edges are sorted after Bonferroni-corrected *p*-values. *"R"/"L"* stands for *"Right"/"Left"*, while *"G"* stands for *"Gyrus"*. The *p*-values come from two-sample *t*-tests on Fisher-transformed Pearson correlation coefficients. The last two columns show group averages of the Fisher-transformed Pearson correlation coefficients. The majority of edges with significantly different connectivity had either a low or negative correlation in BOLD, which was further attenuated in dfMRI.

	Edge		**Group average conn.**	
Corr. *p*-value	**ROI 1**	**ROI 2**	**SE BOLD**	**ADC**
3T				
0.00116	R frontal pole	R Cerebral White Matter	-0.324	0.136
0.00525	L posterior insula	R Hippocampus	0.135	-0.199
0.00708	L middle frontal G	R middle frontal G	0.957	0.439
0.00899	L posterior insula	R anterior insula	0.177	0.009
0.01487	R central operculum	L anterior insula	0.255	-0.036
0.01584	L triangular part of inferior frontal G	R triangular part of inferior frontal G	0.748	0.207
0.02677	R posterior insula	L anterior insula	0.239	-0.116
0.03775	L frontal pole	R Cerebral White Matter	-0.377	0.091
0.09396	L posterior insula	R posterior insula	0.222	-0.086
0.13664	L triangular part of inferior frontal G	R middle frontal G	0.599	0.149
0.15088	L triangular part of inferior frontal G	L Cerebral White Matter	-0.31	0.099
0.1764	R Hippocampus	L Cerebral White Matter	0.048	-0.326
0.18471	R posterior insula	L Cerebral White Matter	-0.034	-0.381
0.20447	L superior frontal G	R posterior insula	-0.309	0.04
0.26652	R posterior insula	R middle frontal G	-0.354	-0.013
0.38503	R middle frontal G	L inferior occipital G	-0.226	0.008
0.39822	R posterior insula	L frontal operculum	0.105	-0.076
0.39847	R superior frontal G	R posterior insula	-0.307	0.039
0.42543	L planum polare	R Hippocampus	0.117	-0.144
0.50374	R posterior insula	L inferior occipital G	0.096	-0.089
7T				
0.00004	L lingual G	R lingual G	1.169	0.485
0.00403	L middle frontal G	R lingual G	-0.483	-0.05
0.01228	R central operculum	L anterior insula	0.152	-0.224
0.01941	R planum polare	L central operculum	0.289	-0.1
0.01985	R superior frontal G medial segment	L Pallidum	-0.367	0.046
0.03117	R lingual G	L frontal operculum	-0.4	-0.086
0.04015	L opercular part of inferior frontal G	R Cerebral White Matter	-0.656	-0.266
0.04457	R superior frontal G medial segment	R lingual G	-0.446	-0.038
0.06359	L lingual G	L frontal operculum	-0.444	-0.125
0.07286	R triangular part of inferior frontal G	L lingual G	-0.505	-0.147
0.07396	L anterior cingulate G	L Pallidum	-0.37	0.057
0.07722	R triangular part of inferior frontal G	L inferior occipital G	-0.36	0.008
0.09221	L middle frontal G	L lingual G	-0.566	-0.141
0.09886	L posterior insula	R central operculum	0.252	-0.116
0.10686	R inferior occipital G	R frontal pole	-0.281	0.065
0.11826	L frontal operculum	R central operculum	0.136	-0.148
0.12879	R anterior cingulate G	L Pallidum	-0.405	0.057
0.15875	R frontal operculum	L anterior insula	0.379	-0.045
0.17333	R superior frontal G medial segment	L lingual G	-0.501	-0.106
0.17351	R superior frontal G medial segment	L Putamen	-0.241	0.07